Realization of Bullard's disc dynamo

Avalos-Zúñiga, R. & Priede, J.

Published PDF deposited in Coventry University's Repository

Original citation:
Avalos-Zúñiga, R & Priede, J 2023, 'Realization of Bullard's disc dynamo', Proceedings of the Royal Society A: Mathematical, Physical and Engineering Sciences, vol. 479, no. 2271. https://doi.org/10.1098/rspa.2022.0740

DOI 10.1098/rspa.2022.0740
ISSN 1364-5021
ESSN 1471-2946

Publisher: The Royal Society

© The Authors. Published by the Royal Society under the terms of the Creative Commons Attribution License http://creativecommons.org/licenses/by/4.0/, which permits unrestricted use, provided the original author and source are credited.

arXiv:2211.03377v3 [physics.geo-ph] 9 Mar 2023

PROCEEDINGS A

rspa.royalsocietypublishing.org

Research

Check for updates

Article submitted to journal

Subject Areas:
electromagnetism

Keywords:
disc dynamo, homopolar generator, geomagnetism

Author for correspondence:
J. Priede
e-mail: j.priede@coventry.ac.uk

Realization of Bullard's disc dynamo

Raúl Alejandro Avalos-Zúñiga[1], Jānis Priede[2,3]

[1]Research Centre in Applied Science and Advanced technology, Instituto Politécnico Nacional (CICATA - Querétaro), Cerro Blanco 141, Colinas del Cimatario, Querétaro, Mexico
[2]Fluid and Complex Systems Research Centre, Coventry University, Coventry, CV1 5FB, United Kingdom
[3]Department of Physics, University of Latvia, Riga, LV-1004, Latvia

We report experimental results from three successful runs of a Bullard-type homopolar disc dynamo. The set-up consisted of a copper disc with a radius of $30\,\mathrm{cm}$ and thickness of $3\,\mathrm{cm}$ which was placed co-axially beneath a flat, multi-arm spiral coil of the same size and connected to it electrically at the centre and along the circumference by sliding liquid-metal contacts. The magnetic field was measured using Hall probes which were fixed on the top face of the coil. We measured also the radial voltage drop across the coil. When the disc rotation rate reached $\Omega \approx 7\,\mathrm{Hz}$, the magnetic field increased steeply approaching $B_0 \approx 40\,\mathrm{mT}$ in the central part of the coil. This field was more than two orders of magnitude stronger than the background magnetic field. In the first two runs, the electromagnetic torque braking the disc in the dynamo regime exceeded the breakdown torque of the electric motor driving the disc. As a result, the motor stalled and the dynamo was interrupted. Stalling did not occur in the third run when the driving frequency was set higher and increased faster. We also propose an extended disc dynamo model which qualitatively reproduces the experimental results.

© The Authors. Published by the Royal Society under the terms of the Creative Commons Attribution License http://creativecommons.org/licenses/by/4.0/, which permits unrestricted use, provided the original author and source are credited.

THE ROYAL SOCIETY PUBLISHING

1. Introduction

Bullard's disc dynamo [1] is arguably the simplest model of the magnetohydrodynamic dynamo. It is often used to illustrate the self-excitation of the magnetic field by moving conductors [2]. This is how the magnetic fields of the Earth, the Sun and many other cosmic bodies are thought to come about [3]. In its basic form, the Bullard dynamo consists of a solid metal disc and a wire: the former spinning about its central axis and the latter twisted around and connected through sliding contacts to the rim and axis of the disc. If the disc spins sufficiently fast and in the right direction, such a set-up can amplify the electric current circulating in the system and, thus, the associated magnetic field. This happens when the rotation rate of the disc exceeds a certain critical threshold above which the potential difference induced across the disc exceeds the voltage drop caused by the ohmic resistance of the system. Then the current starts to grow exponentially in time resulting in the self-excitation of the magnetic field. The growth stops when the braking electromagnetic torque becomes so strong that it slows down the disc. This is how the dynamo would operate in the ideal case with no background magnetic field.

In the presence of a background magnetic field, the dynamo may manifest itself somewhat differently. In this case, a current is induced in the set-up as soon as the disc starts to rotate. If the disc rotates in the right direction, the induced current amplifies the background magnetic field which, in turn, amplifies the current. Thus, the rate of amplification increases with the speed of rotation and becomes formally infinite at the dynamo threshold.

Despite its simplicity, the implementation of the disc dynamo is faced with severe technical challenges. The main problem is the sliding electrical contacts which are required to convey the current between the rim and the axis of the rotating disc. The electrical resistance of sliding contacts, which are usually made of solid graphite brushes, is typically several orders of magnitude higher than that of the rest of the set-up. This results in unrealistically high rotation rates which are required for the dynamo to operate. Therefore, in contrast to the fluid dynamos, which have been realised in several laboratory experiments using liquid metal [4, 5, 6] ([7] in preparation), the disc dynamo was thought to be technically unfeasible [8, 9, 10].

We overcome this problem by using sliding liquid-metal electrical contacts which are similar to those employed previously in the homopolar motors and generators [11, 12, 13] as well as in the laboratory model of Herzenberg dynamo [14] built by Lowes and Wilkinson [15, 16]. The set-up consists of a coil made of a stationary copper disc which is divided into spiral-shaped sections by thin slits [17]. The coil is placed co-axially above the solid copper disc and connected to the latter by sliding liquid-metal contacts. The slits make the conductivity of the coil anisotropic which allows this essentially axially symmetric dynamo to generate an axially symmetric magnetic field [18, 19].

In this paper, which is organised as follows, we report results from three successful runs of such a dynamo. Set-up is described in Sec. 2. Experimental results are presented in Sec. 3. In Sec. 4, we introduce an extended disc dynamo model which is used in Sec. 5 for the interpretation and analysis of experimental results. Summary and conclusions are presented in Sec. 6.

2. Experiment set-up

The dynamo set-up shown in Fig. 1 consists of a rotating copper disc and a coil. The latter is made of a flat copper cylinder of radius $r_o = 30\,\mathrm{cm}$ and thickness $d = 3\,\mathrm{cm}$ which is sectioned starting from the radius $\tilde{r}_i = 7.5\,\mathrm{cm}$ by 40 logarithmic spiral slits with a constant pitch angle $\alpha \approx 58^\circ$. The disc has an annular channel along the rim and a cylindrical cavity at the centre. The coil, which has a cylindrical solid electrode protruding $4\,\mathrm{cm}$ out from the centre of its bottom face, is placed $3\,\mathrm{mm}$ above the disc. At the inner and outer radii, $r_i = 4.5\,\mathrm{cm}$ and $r_o = 30\,\mathrm{cm}$, there are two annular gaps of width $\delta = 0.25\,\mathrm{mm}$ and height $d = 3\,\mathrm{cm}$ which separate the coil from the disc. These gaps were filled with the eutectic alloy of $GaInSn$, which is liquid at room temperature. The coil and

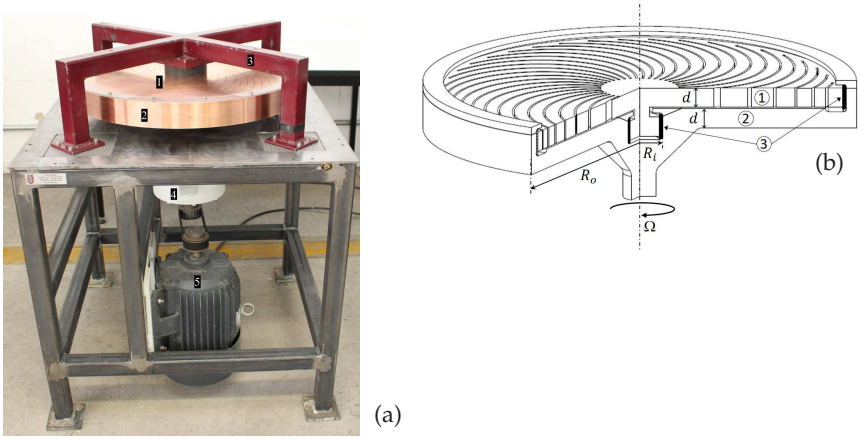

Figure 1. (a) Set-up consisting of coil (1), disc (2), iron frame (3), gearing system (4), and AC motor (5); (b) a cross-sectional view showing coil (1), disc (2), and sliding liquid-metal contacts (3).

disc are held by electrically insulated iron supports. Note that, in the initial design with $3\,\mathrm{mm}$ annular gaps, electrical contacts failed before the dynamo threshold was attained [20].

The disc was driven by a $3\,\mathrm{HP}$ $(2.2\,\mathrm{kW})$ 6-pole AC motor which had a synchronous rotation rate of $1200\,\mathrm{RPM}$ at $60\,\mathrm{Hz}$ input frequency. The sense of rotation was opposite to the orientation of the spiral arms of the coil which corresponds to a clock-wise rotation in the set-up shown in Fig. 1(b). The rotation rate was changed using a variable frequency drive (VFD) Delta VFD022EL23A with a rated output current of $11\,\mathrm{A}$. The VFD output frequency was controlled from a PC using the LabVIEW software. With default settings, the output voltage was reduced directly with the driving frequency. In this standard VFD regime, the driving torque was maintained constant while the motor power dropped off directly with the rotation rate. It means that the maximal power the motor can produce, when operated sufficiently close to the expected dynamo threshold of $600\,\mathrm{RPM}$ $(10\,\mathrm{Hz})$, is only half of its rated power, i.e., $\approx 1\,\mathrm{kW}$. The actual output power may be significantly lower when the rotation rate starts to drop because of too high a load.

The rotation rate was determined using a self-made opto-mechanical tachometer which consisted of a disc with periodic slits with a light source on one side and a photodiode on the other. The magnetic field was measured using the THM1176 3-axis Hall Magnetometer of Metrolab with the low- and medium-field probes THM1176-LF and THM1176-MF. These probes have an active volume and the upper magnetic field strength of $6\times3.4\times3\,\mathrm{mm}^3$,$8\,\mathrm{mT}$ and $16.5\times5\times2.3\,\mathrm{mm}^3$, $100\,\mathrm{mT}$, respectively. The probes were fixed with adhesive tape on the upper face of the coil next to one of the crossed iron arms holding the coil. Three components of field were acquired for a period of several minutes at the rate of 30 samples per second. The voltage between the inner and outer radii of the spiral arms was measured using a digital multimeter Keithley 2100.

3. Experimental results

In this section, we present experimental results for three runs in which the disc rotation rate was measured together with the induced voltage and the magnetic field at the upper face of the coil. The runs differ mainly by the way in which the frequency driving the motor was varied. In the first run, for which the results are shown in the top row of Fig. 2, the driving frequency was ramped up from zero to $\Omega_d = 7.33\,\mathrm{Hz}$ nearly linearly in $\approx 79\,\mathrm{s}$. Although the rotation rate Ω closely followed Ω_d, there was a difference between both frequencies. This difference increased as the magnetic field became stronger. In this run, the magnetic field was measured using only the low-field probe which was placed in the vicinity of the inner radius of the spiral slits. Before the disc started to rotate, a background field $\vec{B}_0 \approx -(0.18, 0.77, 0.57)\,\mathrm{mT}$ with y component directed

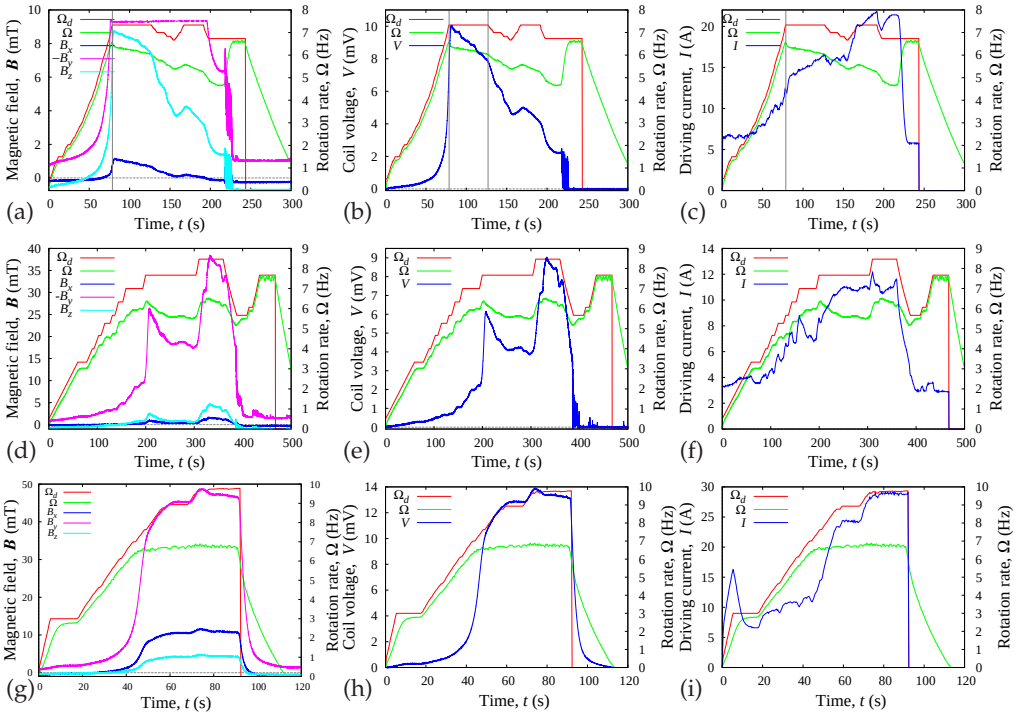

Figure 2. The magnetic field (B_x, B_y, B_z) at the inner radius of the coil (a,d,g), the voltage between the centre and the rim of the coil (b,e,h), and the electric current supplied to the motor (c,f,i) along with the driving (Ω_d) and rotation (Ω) frequencies recorded during the first (a,b,c), second (d,e,f) and third (g,h,i) runs.

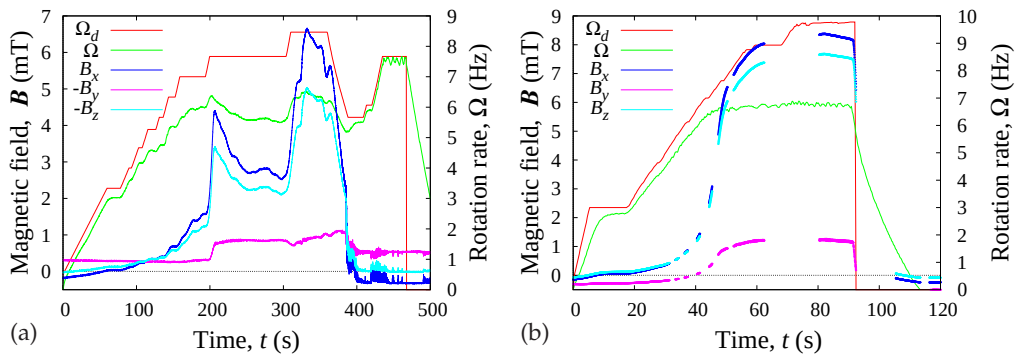

Figure 3. The magnetic field (B_x, B_y, B_z) at the outer radius of the coil along with the driving (Ω_d) and rotation (Ω) frequencies in the second (a) and third (b) runs.

downwards and x and z components in the plane of the coil was detected. This field, which was more than an order of magnitude stronger than Earth's magnetic field, was obviously due to the iron frame holding the coil.

As the rotation rate increased, the magnetic field raised steeply, especially its vertical (y) component, which is seen Fig. 2(a) to exceed the upper limit of the low-field Hall sensor by reaching $B_y \approx -9.3\,\mathrm{mT}$ at $\Omega \approx 6.5\,\mathrm{Hz}$ $(t \approx 76\,\mathrm{s})$. A few seconds later, the increase in the driving frequency was halted at $\Omega_d = 7.33\,\mathrm{Hz}$. At this point, the rotation rate, which had reached $\Omega \approx 6.7\,\mathrm{Hz}$, started to fall while the x and z components of the magnetic field kept growing for a

few more seconds. The same held also for the coil voltage which can be seen in Fig. 2(b) to rise from $V \approx 7.7\,\mathrm{mV}$ at the velocity maximum to $V_{\max} \approx 10\,\mathrm{mV}$ at $t \approx 82\,\mathrm{s}$. However, this time delay between the rotation rate and the other two measured quantities was too short to be determined reliably. Namely, it was comparable to the uncertainty in the time synchronization between the measurements of these quantities which were recorded using different devices.

The slowdown means that the electromagnetic braking torque acting on the disc had shot past the equilibrium point corresponding to the driving torque produced by the motor. As discussed before, this effect can be due to transient eddy currents which, according to the previous estimates, decay over the characteristic time $\sim 1\,\mathrm{s}$. They reduce the magnetic flux through the disc and so the associated electromagnetic braking torque when the disc accelerates while the opposite is the case when the disc decelerates. Although the decrease in the rotation rate at the fixed driving frequency and voltage results in the rise of the current running through the motor (seen in Fig. 2c), it does not prevent the slowdown because the maximal torque the motor can develop is lower than the electromagnetic braking torque. Actually, the deceleration is escalated further by the relatively large difference between the driving and rotation frequencies. When the frequency difference becomes too large, the motor breaks down because the output torque, which is described by Eq. (4.14), starts dropping with the rotation rate.

Although, as seen in Fig. (2c), the coil voltage drops together with the rotation frequency, the rate of decrease is lower than that at which the voltage increased when the disc accelerated. Both the voltage and the magnetic field are noticeably higher than the respective values at the same rotation rate in the acceleration stage. This difference is likely due to the remanent magnetization of the iron frame. However, the transient eddy currents, which delay the variation of the magnetic flux through the disc as discussed above, can have a similar effect.

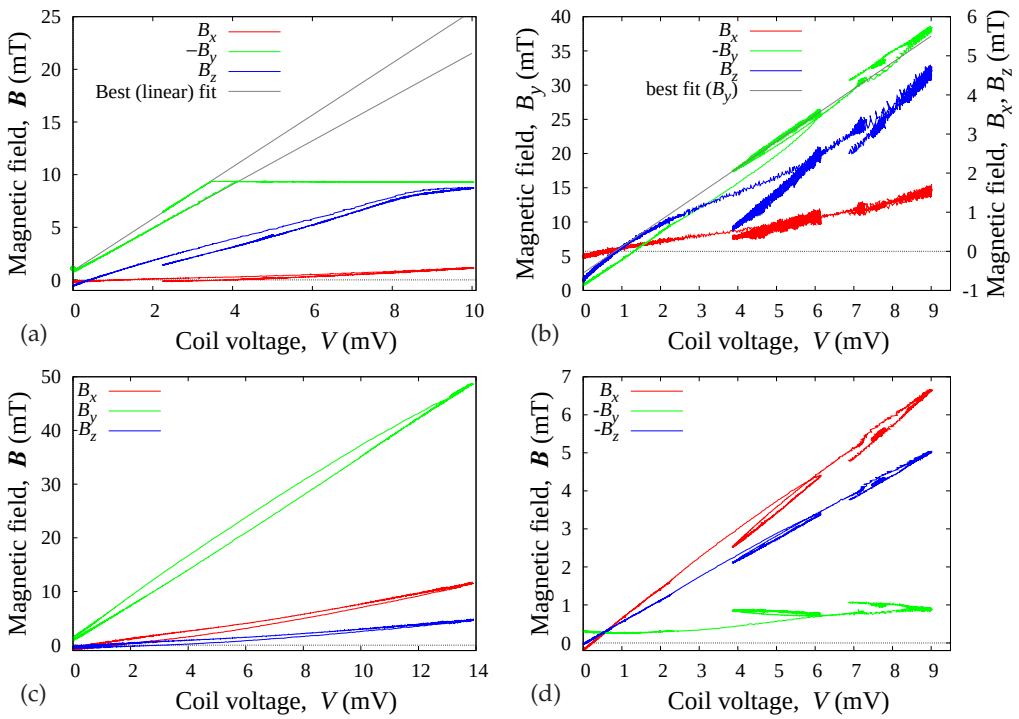

Figure 4. The magnetic field at the inner radius of spiral slits for three runs (a,b,c) and at the outer radius for the second run (d) versus the coil voltage.

Attempting to reduce the slip, at $t \approx 126\,\mathrm{s}$, we started to ramp down Ω_d to $7\,\mathrm{Hz}$ which was reached in $\approx 7\,\mathrm{s}$. This, however, just increased the slowdown rate without noticeably reducing the slip. The subsequent reduction of Ω_d to $6.7\,\mathrm{Hz}$ had a similar effect. The slowdown temporarily reversed at $t \approx 156\,\mathrm{s}$ when Ω_d was ramped up to the original level of $7.33\,\mathrm{Hz}$. Acceleration lasted only for $\approx 15\,\mathrm{s}$ after which Ω resumed falling. When, at $t \approx 192\,\mathrm{s}$, Ω_d was ramped down in $\approx 6\,\mathrm{s}$ to $6.73\,\mathrm{Hz}$, the falling rate of rotation frequency as well as that of the magnetic field initially increased. After $\approx 6\,\mathrm{s}$, when the rotation rate and the y component of the magnetic field had dropped down to $\Omega \approx 1.6\,\mathrm{Hz}$ and $B_y \approx 5.6\,\mathrm{mT}$, the slowdown stopped and the disc started to re-accelerate. Unfortunately, a few seconds later, the liquid metal contacts started to fail due to the excessive oxidation caused by the exposure to the air. The failure started with sporadic current interruptions which appear as irregular oscillations of the magnetic field and coil voltage in Figs. 2(a,b). The electric contact vanished completely in $\approx 8\,\mathrm{s}$ and so did the associated electromagnetic braking torque. As a result, the disc quickly accelerated to the prescribed VFD frequency, and the motor current dropped from $\approx 21\,\mathrm{A}$ to $5.7\,\mathrm{A}$ (see Fig. 2c). The motor was turned off at $t \approx 244\,\mathrm{s}$ and slowed down by the VFD linearly to a complete stop in $\approx 60\,\mathrm{s}$. The magnetic field measured at this point, $\vec{B}_0 \approx -(0.23, 1.0, 0.72)\,\mathrm{mT}$, was $26 - 36\%$ higher than at the beginning of the run. This difference is obviously due to the remanent magnetization of the iron frame.

The peak value of B_y, which was not measured because it exceeded the upper detection limit of the low-field Hall probe, can be estimated by extrapolating its variation with the coil voltage. In a quasi-stationary regime, both the voltage and the associated magnetic field are expected to vary linearly with the current. This is confirmed by their mutual dependence plotted in Fig. 4(a). Extrapolating the rising part of $V$and B_y, which corresponds to the lower branch, we have $B_y \approx 22\,\mathrm{mT}$ at the maximal coil voltage $V \approx 10\,\mathrm{mV}$. Extrapolating the falling part, which corresponds to the upper branch, we respectively have $B_y \approx 25\,\mathrm{mT}$. The dependence of the magnetic field on its direction of variation is most likely due to the remanent magnetization of the iron frame.

It is interesting to note that the relation between the coil voltage and the magnetic field is nearly linear except the z component which appears to saturate close to $9\,\mathrm{mT}$,i.e., the upper detection limit of the low-field Hall probe. Also note that both the iron frame and the spiral slits made the magnetic field strongly non-uniform at the inner and outer edges of the coil where the probes were placed. As a result, the strength, as well as the direction of the magnetic field, were found to vary noticeably with the location of the Hall sensor which was not fixed and may vary between the runs.

In the second run, the low-field probe was moved to the outer radius and the medium-field probe was placed near the inner radius of the coil. The driving frequency was ramped up through intermediate steps rather than continuously as in the first run. As seen in Fig. 2(d,e), this resulted in the rise of the magnetic field and the coil voltage at an increasing rate. A particularly steep increase was observed when Ω_d was ramped up from $7\,\mathrm{Hz}$ at $t \approx 194\,\mathrm{s}$ to $7.67\,\mathrm{Hz}$ at $t \approx 200\,\mathrm{s}$. As the rotation rate increased from $6.1\,\mathrm{Hz}$ to $6.4\,\mathrm{Hz}$, $B_y$at the inner radius rose steeply from $9.5\,\mathrm{mT}$ up to $26.5\,\mathrm{mT}$. The magnetic field at the outer radius can be seen in Fig. 3 to increase in a similar way. The coil voltage, which is plotted Fig. 2(e), increased respectively from $2.2\,\mathrm{mV}$ to $6.1\,\mathrm{mV}$. After that the rotation rate started to fall and so did the magnetic field along with the coil voltage. It indicates that the electromagnetic braking torque had again exceeded the torque that the motor can produce at the given parameters. Thus, the motor was not able to sustain the previously attained field strength and went into the breakdown regime. The rotation rate kept falling until $\Omega \approx 5.6\,\mathrm{Hz}$ was reached at $t \approx 255\,\mathrm{s}$. At this point, the slowdown ended and the rotation rate started to increase slowly. This increase lasted only for $t \approx 25\,\mathrm{s}$ after which the rotation rate dropped again reaching $\Omega \approx 5.5\,\mathrm{Hz}$ at $t \approx 297\,\mathrm{s}$. The subsequent increase in the rotation rate was enhanced at $t \approx 304\,\mathrm{s}$ by ramping up the driving frequency to $8.47\,\mathrm{Hz}$ which was reached in $\approx 6\,\mathrm{s}$. As a result, the rotation rate raised forming a plateau at $t \approx 315\,\mathrm{s}$ with $\Omega \approx 6.3\,\mathrm{Hz}$ which lasted for $\approx 8\,\mathrm{s}$. The vertical magnetic field, which is shown in Fig. 2(d), reached $B_y \approx 30\,\mathrm{mT}$ at $t \approx 319\,\mathrm{s}$ and stayed close to this value for $\approx 6\,\mathrm{s}$. After the plateau, the rotation rate can be seen to increase slightly reaching $\approx 6.5\,\mathrm{Hz}$ in $\approx 2\,\mathrm{s}$. This caused a steep rise in the magnetic field which reached a

peak of $\approx 38\,\mathrm{mT}$ at $t \approx 333\,\mathrm{s}$. As before, the motor could no longer sustain the attained rotation rate which, thus, started to fall closely followed by the magnetic field until reaching $\Omega \approx 6.1\,\mathrm{Hz}$ and $B_y \approx 32.5\,\mathrm{mT}$ at $t \approx 359\,\mathrm{s}$. At this point, we started to ramp down the driving frequency thus disrupting the subsequent growth phase. At $t \approx 386\,\mathrm{s}$, when the rotation rate had slowed down to $\Omega \approx 5.2\,\mathrm{Hz}$, oscillations in the magnetic field increased abruptly and the field started to fall sharply. The same may be seen in Fig. 2(e) to happen to the coil voltage. This introduces the breakdown of electric contact which was completely lost at $t \approx 400\,\mathrm{s}$. At this point, the magnetic field dropped down close to its initial background value. As the electromagnetic braking torque vanished, the disc rotation rate increased approaching the VFD driving frequency. Although the motor closely followed the driving frequency in this regime, the VFD caused some oscillations in the rotation rate around $\Omega \approx 7.5\,\mathrm{Hz}$ which may be seen in Figs. 2(d-f).

In the third run, which is documented in Figs. 2(g-j), the driving frequency Ω_d was set higher and ramped up faster than in the second run. Firstly, the driving frequency was ramped up in $5.4\,\mathrm{s}$ to $\Omega_d \approx 3\,\mathrm{Hz}$. Secondly, after $\approx 12\,\mathrm{s}$, when the rotation rate had stabilized at $\Omega \approx 2.8\,\mathrm{Hz}$, the driving frequency was ramped up to $\Omega_d \approx 8.9\,\mathrm{Hz}$, which was reached nearly linearly via a few short intermediate steps at $t \approx 60\,\mathrm{s}$. The motor rotation rate also increased nearly linearly but at a slightly lower pace than the driving frequency and only up to $\Omega \approx 6.7\,\mathrm{Hz}$ which was attained at $t \approx 45\,\mathrm{s}$. At this point, Ω ceased to increase further with Ω_d. The subsequent results show that only the magnetic field was affected by Ω_d while Ω stayed nearly constant. Namely, the magnetic field, which saturated at $B_y \approx 45\,\mathrm{mT}$ when the driving frequency was set to $\Omega_d \approx 8.9\,\mathrm{Hz}$,can be seen in Fig. 2(g) to reach $B_y \approx 48.6\,\mathrm{mT}$ at $t \approx 74\,\mathrm{s}$ when the driving frequency was ramped up $\Omega_d \approx 9.7\,\mathrm{Hz}$. Although B_y fell off subsequently, it remained well above the previous equilibrium level until the motor was switched off at $t \approx 92\,\mathrm{s}$.

4. An extended disc dynamo model

In this section, we extend our original quasi-stationary disc dynamo model [17] by including several effects which are essential for the interpretation and analysis of the experimental results. In order to capture the temporal evolution and saturation of the disc dynamo, first of all, we need to take into account two transient inductive effects. The first is an additional potential difference between the inner and outer rim of the coil which is induced by a time-dependent electric current $I_1(t)$ flowing along the spiral arms of the coil and then connecting radially through the disc. Owing to the fixed distribution of $I_1(t)$ in the coil, this voltage can be expressed analytically in terms of the rate of variation of the associated magnetic flux (Eq. (8) in [17]). The second effect, which is neglected in the original disc dynamo model [1], is the eddy current induced in the disc by a changing magnetic field [21]. The linear density of this purely azimuthal current is governed by Ohm's law

$$J_2(r,t) = \bar{\sigma} E_\phi,$$

where $\bar{\sigma} = \sigma d$ is the effective electric conductivity of the disc and $E_\phi = -\partial_t A_\phi$ is the induced electric field which follows from Faraday's law with A_ϕ standing for the azimuthal component of the vector potential. Using the Biot-Savart law, the latter can be written as follows

$$A_\phi(r,t) = \frac{\mu_0}{4\pi} \int_{\tilde{r}_i}^{r_o} \int_0^{2\pi} \frac{(J_1(r',t) - \bar{\sigma}\partial_t A_\phi) r' \cos\phi}{\sqrt{r^2 + r'^2 - 2rr'\cos\phi}} \,\mathrm{d}\phi\,\mathrm{d}r', \tag{4.1}$$

which is an integro-differential equation governing the evolution of A_ϕ over the radius of the system; $J_1(r,t) = \beta I_1(t)/2\pi r$ stands for the azimuthal current distribution in the coil and $\mu_0 = 4\pi \times 10^{-7}\,\mathrm{H/m}$ is the permeability of vacuum. Note that the vertical gap between the disc and the coil is supposed to be much smaller than the radial size. Thus, the magnetic flux passing through the disc is approximately the same as that passing through the coil [17]. In the following, instead of solving Eq. (4.1), which is numerically complicated, we pursue a simplified approach

by assuming that the aforementioned magnetic flux can be written as

$$\Phi = L_1 I_1 + L_2 I_2 + \Phi_0, \tag{4.2}$$

where the first two terms on the RHS represent the fluxes generated by the coil and the disc, respectively, and Φ_0 is a background flux due to external magnetic which may be Earth's magnetic field as well as to that produced by the magnetized iron frame. This model differs from that of Moffatt [21] first, by taking into account the external field and, second, by neglecting the leakage of the magnetic flux through the gap between the coil and the disc.

Applying Kirchhoff's voltage law to the primary dynamo circuit, which carries the current I_1, and to the disc, which constitutes the secondary circuit, we obtain

$$\dot{\Phi} + R_1 I_1 = \Omega\Phi, \tag{4.3}$$

$$\dot{\Phi} + R_2 I_2 = 0, \tag{4.4}$$

where R_1 and R_2 are the effective ohmic resistances of respective circuits. The system is completed by the angular momentum equation:

$$\mathcal{I}\dot{\Omega} = G - I_1\Phi - k\Omega, \tag{4.5}$$

where $\mathcal{I}$ is the moment of inertia of the disc, G is the driving torque produced by the motor and $I_1\Phi$ is the electromagnetic braking torque [21]. The last term with the coefficient k represents a hyrodynamic-type friction. It can also model the variation of the driving torque with the rotation speed as in asynchronous electric motor controlled by the VFD with a fixed voltage and frequency ratio. The system can be reduced to two equations for Φ and Ω as follows. First, substituting $I_2 = -\dot{\Phi}/R_2$ from Eq. (4.4) into Eq. (4.2) we have

$$I_1 = (\Phi - \Phi_0 + \dot{\Phi}L_2/R_2)/L_1,$$

Second, substituting this expression for I_1 into Eqs. (4.3) and (4.5), after a few rearrangements, we obtain:

$$\tau_0\dot{\Phi} = \Phi(\tau_1\Omega - 1) + \Phi_0 \tag{4.6}$$

$$\mathcal{I}\dot{\Omega} = G - \Phi(\Phi + \tau_2\dot{\Phi})/L_1 - k\Omega, \tag{4.7}$$

where $\tau_i = L_i/R_i$ are the characteristic electromagnetic decay times (the time constants) for the primary $(i = 1)$ and secondary $(i = 2)$ circuits and $\tau_0 = \tau_1 + \tau_2$. Note that the kinematic dynamo problem, which corresponds to a prescribed rotation rate Ω, is posed just by Eq. (4.6). According to this equation, a small initial current perturbation grows exponentially with time if $\Omega > \Omega_c$, where

$$\Omega_c = \tau_1^{-1} \tag{4.8}$$

is a critical rotation rate defining the dynamo threshold. Scaling rotation rate and time with Ω_c and τ_0, respectively, Eqs. (4.6) and (4.7) can be written in the dimensionless form as follows

$$\dot{\Phi} = \Phi(\Omega - 1) + \Phi_0, \tag{4.9}$$

$$\dot{\Omega} = \Gamma(1 - \kappa\Omega) - \Phi\left(\Phi - \Phi_0 - \lambda\dot{\Phi}\right), \tag{4.10}$$

were Γ is a dimensionless driving torque, κ is a friction coefficient defined relative to Γ and $\lambda = \tau_2/(\tau_1 + \tau_2)$ is a parameter defining the relative significance of eddy currents in the disc. In the following, we assume mechanical friction to be negligible, i.e., $\kappa \ll \Gamma$, and use $\kappa = 0$ unless stated otherwise. Finally, using Eq. (4.9) to eliminate $\dot{\Phi}$ on the RHS of Eq. (4.10), we obtain a second-order dynamical system.

If the disc is segmented by spiral slits like the coil, or by radial insulating strips as suggested by Moffatt [21], so that no azimuthal eddy currents can circulate in the disc, we have $\lambda = 0$. In this case, our model, like that of Moffatt [21], reduces to the original Bullard dynamo model [1]. If the disc is solid and well conducting, as in our experiment, so that $\tau_2 \gg \tau_1$, which will be shown in the following, we have $\lambda = 1$.

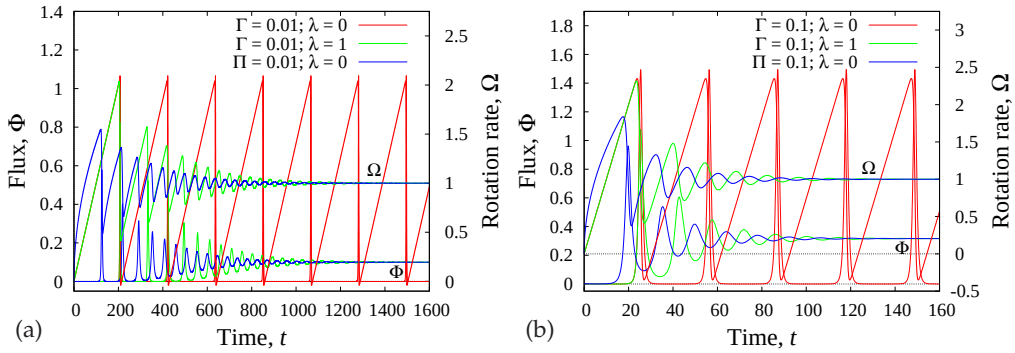

Figure 5. Temporal evolution of the rotation rate and the magnetic flux Φ with a small initial value and no background magnetic field $(\Phi_0 = 0)$ and no mechanical friction $(\kappa = 0)$ when the disc is driven either by a constant torque $\Gamma = 0.1$ (a), 0.01 (b) or a constant power $\Pi = 0.1$ (a), 0.01 (b); λ characterizes the effect of eddy currents in the disc which is negligible when $\lambda = 0$ and significant when $\lambda = 1$.

The driving torque Γ can conveniently be defined using the dynamic response time τ_d, i.e., the time required by the motor to spin up the disc to the critical rotation rate (4.8). In the case of constant driving torque and dominating inertia, Eq. (4.10) yields $\Omega = \Gamma t$. Taking into account that $\Omega_c = 1$, we have $\Gamma = (\tau_d/\tau_0)^{-1}$, which is a dimensionless counterpart of τ_d^{-1}. Similarly, in the case of a constant power $\Pi = \Omega\Gamma$, Eq. (4.10) yields $\frac{1}{2}\Omega^2 = \Pi t$ and, thus, we have $\Gamma = \frac{1}{2}(\Omega\tau_d/\tau_0)^{-1}$.

For a disc of radius r_o and thickness $d \ll r_o$, which can be treated as a thin sheet with the effective electric conductivity $\bar{\sigma} = \sigma d$, the characteristic time over which eddy currents decay can be estimated as $\tau_2 \sim \mu_0 \sigma d r_o$. For our set-up with $r_o = 10d = 0.3\,\mathrm{m}$ and $\sigma = 58.5\,\mathrm{S/m}$, the electromagnetic time constant of the secondary circuit is $\tau_2 \approx 0.7\,\mathrm{s}$.

The time constant of the primary circuit τ_1 can be estimated using Eq. (4.8) and the corresponding critical magnetic Reynolds number, which can be written as follows

$$Rm_c = \mu_0 \sigma d r_o \Omega_c = \tau_2/\tau_1.$$

Then taking into account that $Rm_c \approx 40$ [17], we have $\tau_2 = \tau_1 Rm_c \gg \tau_1$ and, thus, $\lambda \approx 1$.

The characteristic mechanic response time in which the disc attains the expected critical rotation frequency $f_c \approx 10\,\mathrm{Hz}$ when the motor is run at $P \approx 1\,\mathrm{kW}$, i.e. half of its rated power, can be estimated as

$$\tau_d = \frac{1}{2}\mathcal{I}\Omega_c^2/P \approx \pi^3 \rho d r_o^4 f_c^2/P \approx 7\,\mathrm{s},$$

where $\rho = 8.96 \times 10^3\,\mathrm{kg/m^3}$ is the density of copper. This time being by an order of magnitude longer than the electromagnetic response time τ_1 corresponds to $\Gamma \sim 0.1$.

There are two distinct ways how the dynamo can manifest itself. In the classical scenario, the background field is assumed to be absent $(\Phi_0 = 0)$. In this case, as soon as the rotation rate exceeds $\Omega_c = 1$, the magnetic field starts to grow exponentially in time at the rate $\Omega - 1$. This scenario, which corresponds to an instability of the base state $\Phi = 0$ at $\Omega > 1$, is captured by Eqs. (4.9,4.10) with the initial conditions $\Omega(0) = 0$ and $\Phi(0) = \Phi_1$, where Φ_1 is a small initial perturbation.

The second scenario, which more adequately describes the experiment, involves a non-zero background flux Φ_0. In this case, Eq. (4.9) for a fixed rotation rate Ω has a stationary solution $\Phi = \Phi_0/(1-\Omega)$, which shows that the magnetic flux increases with the rotation rate as $\sim (1-\Omega)^{-1}$ and becomes unbounded when $\Omega \to 1$. This is how the dynamo manifests itself in the second scenario.

In reality, the growth of the magnetic field is limited by the electromagnetic braking torque which at a certain point outweighs the driving torque. The stationary solution for the flux defined

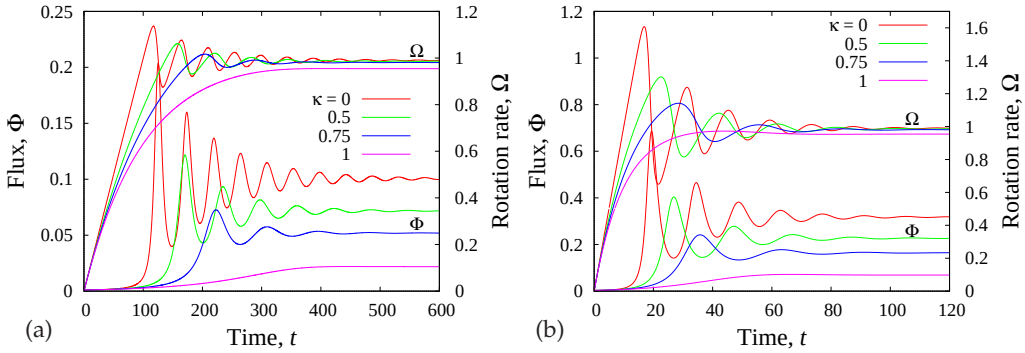

Figure 6. Temporal evolution of the rotation rate and the magnetic flux Φ in the presence of a background field with $\Phi_0 = 0.01\Gamma^{1/2}$, $\lambda = 1$, $\kappa = 0, 0.5, 0.75, 1$ when the disc is driven by a constant torque $\Gamma = 0.01$ (a), 0.1 (b).

by Eq. (4.10) is

$$\bar{\Phi} = \Phi_0/2 + \sqrt{\Phi_0^2/4 + \Gamma}. \tag{4.11}$$

The respective equilibrium rotation rate following from Eq. (4.9) is $\bar{\Omega} = 1 - \Phi_0/\bar{\Phi}$. If the background field is negligible, which is the case when $\Phi_0 \ll \Gamma^{1/2}$, this equilibrium rotation rate becomes equal to the threshold value $\Omega_c = 1$. It means that in this case, the driving torque changes only the equilibrium magnetic flux $\bar{\Phi} = \Gamma^{1/2}$ but not the disc rotation rate which stays equal to $\Omega_c = 1$ [1]. It is important to note, however, that in the Bullard model, which corresponds to a constant driving torque Γ with $\lambda = \Phi_0 = 0$, this equilibrium is never reached and the dynamo keeps oscillating around the equilibrium state unless it coincides with the initial state [1]. Periodic oscillations of the Bullard dynamo are due to an energy-like conserved quantity:

$$(\Omega - 1)^2 + \Phi^2 - \Gamma \ln \Phi^2 = \text{const},$$

which makes Eqs. (4.9, 4.10) integrable. This is no longer the case when the dynamo is driven by a constant power $\Pi = \Omega\Gamma$, which also acts as a mechanical damping. Namely, for small-amplitude oscillations around the equilibrium rotation rate with $\Omega = 1 + \tilde{\Omega}$, we have

$$\Gamma = \Pi/\Omega \approx \Pi - \Pi\tilde{\Omega},$$

where the term Π represents the constant part of the driving torque whereas the term $-\Pi\tilde{\Omega}$ is equivalent to the damping with a coefficient equal to Π. There are two additional electromagnetic damping effects in the modified Bullard dynamo model. They become obvious when Eqs. (4.9, 4.10) are combined into the following equation for small-amplitude magnetic flux perturbation $\tilde{\Phi} = \Phi - \bar{\Phi}$ around the equilibrium flux defined by Eq. (4.11):

$$\partial_t^2\tilde{\Phi} + \tilde{\kappa}\partial_t\tilde{\Phi} + (2\bar{\Phi}^2 - \Phi_0\bar{\Phi})\tilde{\Phi} = 0.$$

This equation features an effective damping coefficient

$$\tilde{\kappa} = \lambda\bar{\Phi}^2 + \Phi_0/\bar{\Phi} \tag{4.12}$$

with the two terms on the RHS being due to the eddy currents induced in the disc and the background magnetic flux, respectively.

The temporal evolution of the rotation rate and the magnetic flux when the disc is driven either by a constant torque Γ or power Π with no background magnetic field ($\Phi_0 = 0$) and negligible friction ($\kappa = 0$) is shown in Fig. 5 for the eddy current parameter $\lambda = 0$ and $\lambda = 1$.

The effect of a background magnetic field with $\Phi_0 = 0.01\Gamma^{1/2}$ on the evolution of the dynamo driven by a constant torque with various friction coefficients is illustrated in Fig. 6. The characteristic feature of the temporal evolution of disc dynamo, which is present in all cases

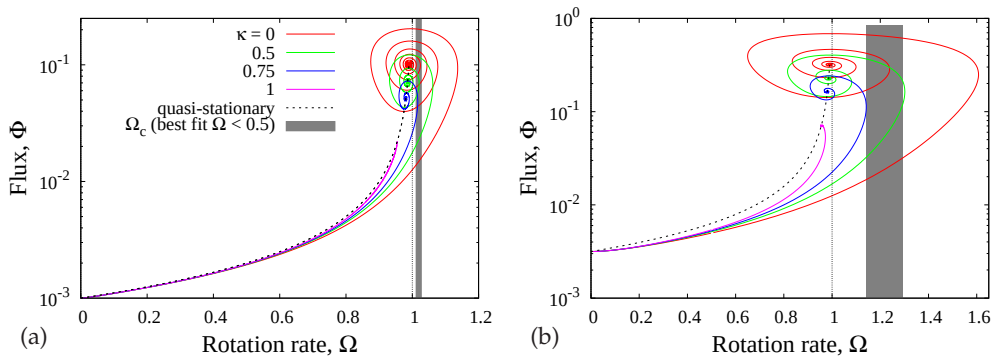

Figure 7. The magnetic flux Φ versus the rotation rate from Fig. 6 along with the quasi-stationary solution (4.13) for $_c = 1$ and $\Gamma = 0.01$ (a), 0.1 (b). The shaded strips show the range of $_c$ resulting from the best fit of numerical results for various κ and $\leq$ $_c/2$, where the solution is relatively quasi-stationary.

except the marginal case of $\kappa = 1$, is the overshooting of the equilibrium state and the subsequent oscillations of the rotation rate and the magnetic flux. These oscillations, which decay unless $\kappa = \lambda = 0$ and the dynamo is driven by a constant torque, imply that deviation from the quasi-stationarity becomes significant when the disc rotation rate approaches the dynamo threshold $\Omega_c = 1$. This is because the effective magnetic relaxation time being reciprocal of the growth rate diverges as $\sim (\Omega_c - \Omega)^{-1}$ when Ω approaches Ω_c. As a result, the quasi-stationarity inevitably breaks down in the vicinity of the dynamo threshold regardless of how slowly the rotation rate is ramped up. Deviation from the quasi-stationary solution of Eq. (4.9):

$$\Phi(\Omega) = \frac{\Phi_0}{\Omega_c - \Omega}, \tag{4.13}$$

becomes obvious when the magnetic flux is plotted against the rotation rate as in Fig. 7. This numerical data can be used to assess the possibility of recovering Ω_c from the best fit to the quasi-stationary solution. Limiting the fit to $\Omega \leq \Omega_c/2$, where the solution is relatively quasi-stationary, we recover the values of Ω_c which slightly vary with κ and lie in the shaded strips Fig. 7. As seen, Ω_c produced by the best fit is just slightly higher than the true value $(\Omega_c = 1)$ for $\Gamma = 0.01$ whereas the difference is about 20% when $\Gamma = 0.1$.

When the dynamo is powered by an induction motor supplied with constant frequency and voltage, the developed torque varies non-monotonously with the rotation rate. The torque predicted by the basic asynchronous electric motor model [22] can be written as

$$\Gamma = 2\Gamma_{\max} \frac{(\Omega_d - \Omega)(\Omega_d - \Omega_m)}{(\Omega_d - \Omega)^2 + (\Omega_d - \Omega_m)^2}, \tag{4.14}$$

where Ω_d and Ω are the synchronous and actual rotation frequencies, Ω_m is the frequency at which the torque attains its peak value $\Gamma_{\max}$. When $\Omega \approx \Omega_d$, the torque varies approximately linearly with $\Omega_d - \Omega$:

$$\Gamma \approx 2\Gamma_{\max} \frac{\Omega_d - \Omega}{\Omega_d - \Omega_m}.$$

When the frequency difference $\Omega_d - \Omega$ becomes sufficiently large, the driving torque attains a maximum $\Gamma_{\max}$ at the critical frequency Ω_m and then drops off asymptotically as

$$\Gamma \sim 2\Gamma_{\max} \frac{\Omega_d - \Omega_m}{\Omega_d - \Omega}.$$

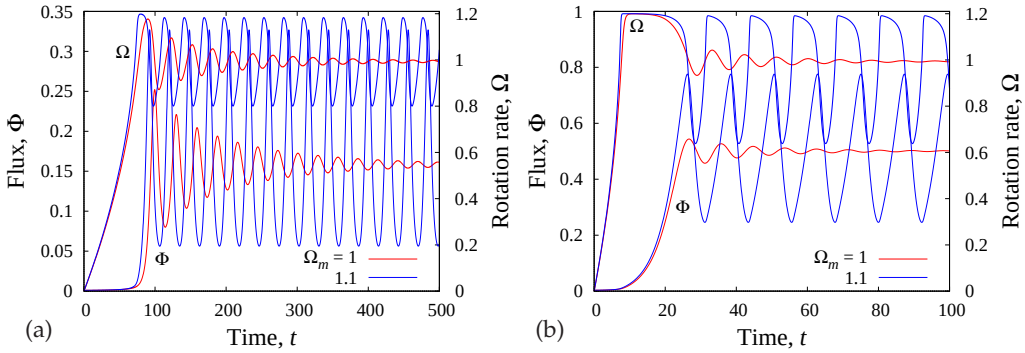

Figure 8. Temporal evolution of the rotation rate and the magnetic flux Φ in the presence of a background field with $\Phi_0 = 0.01\Gamma_{\max}^{1/2}$ and $\lambda = 1$ when the disc is driven by an electric motor with synchronous frequency $_d = 1.2$ and the maximal torque $\Gamma_{\max} = 0.01$ (a), 0.1 (b) developed at $_m = 1,\ 1.1$.

If the equilibrium rotation frequency $\Omega_c = 1$ happens in the latter operating regime, for small perturbations of the rotation rate $\tilde{\Omega} = \Omega - 1$, we have

$$\Gamma \approx 2\Gamma_{\max}\frac{\Omega_d - \Omega_m}{\Omega_d - 1}\left(1 + \frac{\tilde{\Omega}}{\Omega_d - 1}\right),$$

where the second term is analogous to a friction force but with negative coefficient

$$-2\Gamma_{\max}\frac{\Omega_d - \Omega_m}{(\Omega_d - 1)^2}.$$

When this negative friction outweighs the electromagnetic damping with the coefficient (4.12), the stationary dynamo state becomes unstable giving rise to periodic oscillations as in the original Bullard dynamo model. This instability is illustrated in Fig. 8 where the oscillations can be seen to cease decaying when the motor is driven by a fixed frequency $\Omega_d = 1.2$ and the frequency at which the torque attains maximum is increased from $\Omega_m = 1$ to 1.1.

5. Discussion

The measured coil voltage allows us to assess the electric current and the associated ohmic heating. Firstly, using the coil resistance [17]

$$R_c = \frac{1+\beta^2}{2\pi d\sigma_{\mathrm{Cu}}}\ln\frac{r_o}{r_i} \approx 0.61\,\mu\Omega,$$

and the Ohm's law, we can estimate the current generated by the dynamo at the coil voltage $V = 10\,\mathrm{mV}$ as $I = V/R_c \approx 16\,\mathrm{kA}$. Then the associated power of ohmic heating in the coil and disc with the resistivity $R_d = R_c(1+\beta^2)^{-1}$ is

$$P = I^2(R_c + R_d) = \frac{V^2}{R_c}\left(1 + (1+\beta^2)^{-1}\right) \approx 200\,\mathrm{W}. \tag{5.1}$$

This power is significant relative to the maximal power the motor is expected to produce when operating outside its optimal regime with a large slip. Additional, but presumably insignificant, ohmic as well as viscous power dissipation is expected in the liquid metal contacts.

On the other hand, using the current estimate above, the average magnetic flux density produced by the helical coil can be evaluated as

$$\bar{B}_c = \frac{\beta\mu_0 I r_o \bar{\phi}(\tilde{r}_i/r_o)}{4\pi S} \approx 4\,\mathrm{mT}. \tag{5.2}$$

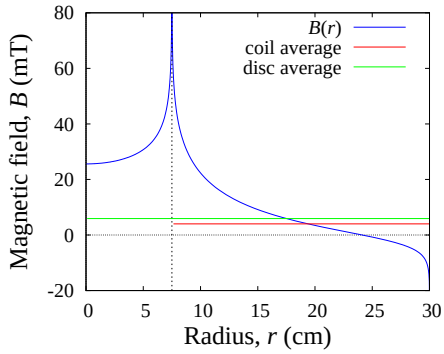

Figure 9. Radial distribution of the vertical magnetic field $B(r)$ along the top surface of the coil computed using a quasi-stationary current-sheet approximation [17] for the coil voltage $V = 10\,\mathrm{mV}$ which corresponds to the dynamo current $I \approx 16\,\mathrm{kA}$. The two horizontal lines show the average values for the coil and disc, respectively.

where $S = \pi(r_o^2 - \tilde{r}_i^2)$ is the area of the helical part of the coil, $\beta = \tan(58^\circ) \approx 1.6$ is the helicity of the logarithmic spiral arms, $\tilde{r}_i/r_o \approx 1/4$ is the ratio of the outer and inner radii of the coil and $\bar{\phi}(1/4) \approx 1.38$ is the respective dimensionless flux [17]. It is interesting to note that this estimate is significantly lower than the magnetic field strength measured on the surface of the coil. There may be several reasons for this difference. Firstly, the distribution of the magnetic field along the surface of the coil is highly non-uniform. In the current-sheet approximation, the vertical flux density $B_z = r^{-1}\partial(rA_\phi)$, which is plotted in Fig. 9 using the analytical solution for the vector potential A_ϕ obtained in [17], becomes unbounded at the inner and outer radii of the coil, where it has logarithmic singularities. Besides that the magnetic flux density can be seen in Fig. 9 to change direction close to the outer edge of the coil. As a result, the average flux density is much lower than the local field strength. Nevertheless, the field strength at the centre of the coil, which represents a well-defined characteristic value for this system, is comparable to the field strength measured in the vicinity of the inner radius of the coil. Secondly, regardless of the current-sheet approximation, there are logarithmic singularities in the field strength at the sharp edges of the coil which may affect the readings of the Hall sensor when placed directly atop the coil.

Thirdly, and most importantly, the magnetic field distribution is strongly affected by the iron frame of the set-up, especially by the four crossed arms holding the coil. . As the Hall sensors were placed on the coil next to these beams, they could be affected by the field concentration caused by these ferromagnetic elements. The effect of the iron frame is evident in the background magnetic field which was found to be $\sim 1\,\mathrm{mT}$, *i.e.*, more than an order of magnitude stronger than Earth's field. This fact implies that the iron frame can have a similar magnitude effect also on the magnetic field generated by the coil.

Given the relative smallness of the coil area covered by the frame, the latter is expected to have a comparably small effect on the average magnetic flux density. This is confirmed by the effective magnetic flux density through the disc B_{eff} which can be estimated by comparing the e.m.f generated by the disc, $\Omega B_{\mathrm{eff}}(r_o^2 - r_i^2)/2$, and the total voltage drop over the disc and coil. The latter can be estimated using the ohmic heating power P (5.1) as P/I, which results in

$$B_{\mathrm{eff}} = 2V\frac{1 + (1+\beta^2)^{-1}}{\Omega(r_o^2 - r_i^2)}. \tag{5.3}$$

As seen in Fig. 10, B_{eff} varies nearly linearly with the coil voltage as predicted by the quasi-stationary approximation well outside this regime. The best fit of this variation for $V < 6\,\mathrm{mV}$ produces an effective flux density of the background magnetic field $\bar{B}_0 = 0.29 \pm 0.03\,\mathrm{mT}$, which is about a factor of three lower than the strength of the background field measured under one of the four iron beams holding the coil.

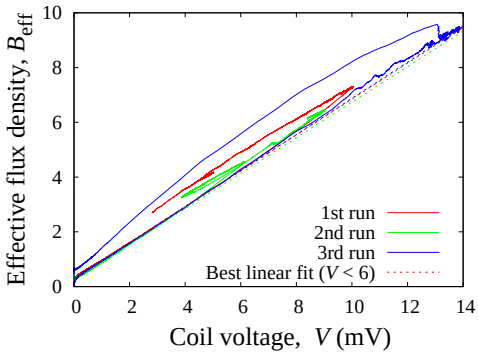

Figure 10. Effective magnetic flux density $B_{\rm eff}$ (5.3) against the coil voltage V for three runs along with the best linear fit $B_{\rm eff} = B_0 + \kappa V$ for $V < 6\,\mathrm{mV}$ which yields $B_0 = 0.29 \pm 0.03\,\mathrm{mT}$.

On the other hand, the effective magnetic flux density, which reaches $B_{\rm eff} \approx 7\,\mathrm{mT}$ at the coil voltage $V = 10\,\mathrm{mV}$, is somewhat higher than $\bar{B}_c$ defined by Eq. (5.2). This difference may be due to the inner radius of the disc $r_i = 4.5\,\mathrm{cm}$ being smaller than the respective radius of the helical part of the coil $\tilde{r}_i = 7.5\,\mathrm{cm}$. As a result, the inner part of the disc with $r < \tilde{r}_i$ is exposed to a relatively strong magnetic field which is generated by the coil in this region (see Fig. 9). On the other hand, the respective magnetic flux density averaged over the whole area of the disc, $\bar{B}_d \approx 6\,\mathrm{mT}$, is relatively close to $B_{\rm eff}$.

The critical frequency Ω_c can be determined by fitting the quasi-stationary solution (4.13), which can be written in terms of the respective quantities as

$$V(\Omega) = \frac{V_0 \Omega}{\Omega_c - \Omega}, \tag{5.4}$$

$$B(\Omega) = \frac{B_0 \Omega_c}{\Omega_c - \Omega}, \tag{5.5}$$

to the variation of the coil voltage and magnetic field with the rotation rate, which is plotted in Fig. 11. Limiting the fit to $\Omega < 6\,\mathrm{Hz}$, where the variation is expected to be sufficiently close to quasi-stationary, and using the coil voltage, we find $\Omega_c \approx 7.2, 6.9, 7.2\,\mathrm{Hz}$ for the respective run (see Fig. 11a). The best fit of the magnetic field yields $\Omega_c \approx 7.0, 6.7, 6.9\,\mathrm{Hz}$, which are somewhat lower than the respective previous values. The last value is also slightly higher than the apparent equilibrium rotation rate in the third run which may be seen in Fig. 2 to reach $\approx 6.8\,\mathrm{Hz}$.

Alternatively, Ω_c can be estimated using the the short equilibrium state which appears in the third run between $t \approx 60\,\mathrm{s}$ and $70\,\mathrm{s}$, where $\Omega \approx 6.8\,\mathrm{Hz}$,$B \approx 45\,\mathrm{mT}$ and $V \approx 12.9\,\mathrm{mV}$. Substituting these values into equations (5.4) and (5.5) and using $B_0 \approx 1.1\,\mathrm{mT}$ and $V_0 \approx 0.45\,\mathrm{mT}$, which follow from the best of B and V for this run, after a few rearrangements, we obtain $\Omega_c = \Omega/(1 - B_0/B) \approx 6.97\,\mathrm{Hz}$ and $\Omega_c = \Omega(1 + V_0/V) \approx 7.0\,\mathrm{Hz}$. As seen both results are practically identical and lying between the values obtained from the best fit of quasi-stationary solutions for V and B. Note that the theoretical dynamo threshold for our set-up, which is defined for negligible contact resistance by the minimal critical magnetic Reynolds number $Rm \approx 35$ [17], corresponds to $\Omega_c \approx 8.2\,\mathrm{Hz}$. Although the background magnetic field makes the equilibrium rotation rate somewhat lower than the self-excitation threshold, the difference between the theoretical threshold and that extracted from the best fit of experimental results may be due to the current sheet approximation used in the theoretical model.

The effective background magnetic field B_0 can also be estimated using the best-fit parameters V_0 and Ω_c of the coil voltage. Substituting V from Eq. (5.4) into Eq. (5.3) and taking $\Omega \to 0$, it is easy see that $\bar{B}_0$ is obtained by replacing V and Ω in Eq. (5.3) with V_0 and Ω_c. For the respective run, this yields $\bar{B}_0 \approx 0.33, 0.26, 0.30\,\mathrm{mT}$, which are consistent with the previous estimate obtained from the best fit of the effective magnetic flux variation with the coil voltage plotted in Fig. 10.

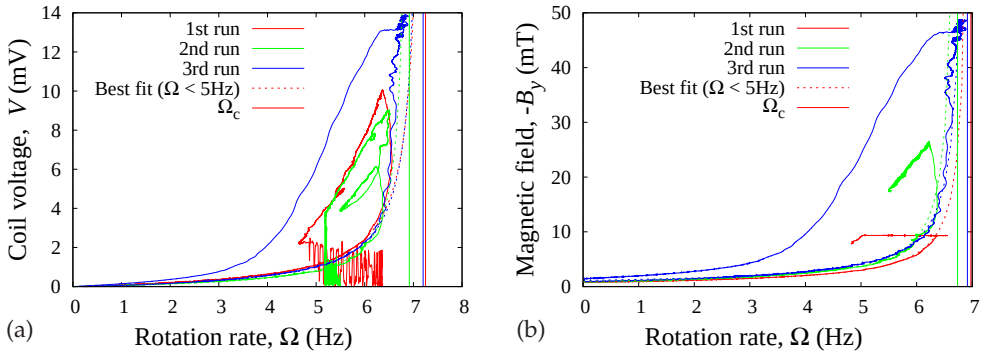

Figure 11. The coil voltage (a) and the vertical component of the magnetic field at the inner radius of the coil (b) versus the rotation rate along with the best fits of the quasi-stationary solution (5.4,5.5) for $< 5\,\mathrm{Hz}$.

The larger scatter in the last estimate is because it is obtained by using low rotation rates only, whereas the previous relation holds in a much larger range of Ω which may be seen in Fig. 10 to extend well beyond the quasi-stationary regime.

6. Summary and conclusions

In this paper, we presented experimental results from three successful runs of a Bullard-type homopolar disc dynamo. The realisation of such a dynamo was commonly thought impossible because of the prohibitively high rotation rates which are required when sliding electric contacts are made of graphite brushes. We overcome this problem by using $GaInSn$ eutectic alloy, which is liquid at room temperature, for sliding electric contacts. The set-up consisted of a copper disc with a radius of $30\,\mathrm{cm}$ and thickness of $3\,\mathrm{cm}$ which was placed co-axially beneath a flat, multi-arm spiral coil of the same size and connected to it electrically at the centre and along the perimeter by $GaInSn$ contacts [17]. The dynamo was effectively axisymmetric but anisotropic because of the spiral slits which deflected the current in the coil azimuthally so generating an axial magnetic field.

The use of liquid metal in sliding electrical contacts came with two complications. Firstly, the liquid metal was expelled from the peripheral contact by centrifugal force radially inwards over the top surface of the coil. This problem was largely mitigated by reducing the annular gap between the disc and the coil from $3\,\mathrm{mm}$ in the original design [20] to $0.25\,\mathrm{mm}$ in this set-up. Secondly, as the liquid metal was exposed to air, it quickly oxidized when the device ran. This limited the time of the experiment to a few minutes after which the electric contact between the disc and the coil usually failed.

The runs differed mainly by how the motor driving frequency Ω_d was varied. In the first run, Ω_d was increased at a nearly constant rate and the magnetic field was measured using only the low-field probe which was placed on the coil in its central part close to the inner radius of the spiral slits. When the disc rotation rate reached $\Omega \approx 6.5\,\mathrm{Hz}$, the vertical field component was found to exceed $9\,\mathrm{mT}$, which was the upper detection limit of this probe. Although the driving frequency was set at $\Omega_d = 7.33\,\mathrm{Hz}$, the rotation rate started to fall after reaching $\approx 6.7\,\mathrm{Hz}$. It means that the electromagnetic torque braking the disc had exceeded the breakdown torque of the electric motor, which, thus, started to stall. Extrapolation using the voltage drop across the coil, which was measured in addition to the magnetic field, indicated that the vertical field strength in the first run had reached $\approx 25\,\mathrm{mT}$. It is important to note that the magnetic field in the vicinity of the inner radius of the coil may be significantly higher than the average over the coil surface.

In the second run, the low-field probe was moved to the outer radius and the medium-field probe was installed in its place. Besides that, the driving frequency was ramped up through intermediate constant steps rather than continuously as in the first run. We again observed a steep increase of the magnetic field with B_y at the inner radius reaching $26.5\,\mathrm{mT}$ when the rotation rate approached $6.4\,\mathrm{Hz}$. At this point, the rotation rate started to fall as in the first run. However, the second run was sufficiently long for the disc to start spinning up again. The re-acceleration was enhanced by ramping up Ω_d to $8.47\,\mathrm{Hz}$. This resulted in Ω reaching $\approx 6.5\,\mathrm{Hz}$ and B_y shooting up to $\approx 38\,\mathrm{mT}$. At this point, the motor started to stall again and the experiment was terminated because of the loss of electric contact.

Stalling was not observed in the third run, in which the driving frequency Ω_d was set higher and initially ramped up faster. With $\Omega_d \approx 8.9\,\mathrm{Hz}$ reached in $\approx 60\,\mathrm{s}$, the rotation rate saturated at $\Omega \approx 6.6 \pm 0.1\,\mathrm{Hz}$ after $\approx 45\,\mathrm{s}$. The magnetic field kept growing as long as Ω_d increased saturating at $\approx 45\,\mathrm{mT}$. After $\approx 30\,\mathrm{s}$, when Ω_d was raised to $\approx 9.7\,\mathrm{Hz}$, B_y increased to $\approx 48.6\,\mathrm{mT}$ without a noticeable change in the rotation rate Ω. This is a characteristic behaviour of a fully developed disc dynamo.

We also proposed an extended disc dynamo model which qualitatively reproduces experimental results by taking into account the background magnetic field, transient eddy currents in the disc as well as the non-linearity of the electric motor. The background magnetic field, which was found to be an order of magnitude stronger than Earth's magnetic field, was obviously due to the iron frame of the set-up. At sub-critical rotation rates, i.e., those below the kinematic threshold, the dynamo works as a homopolar generator amplifying the background magnetic field. In quasi-stationary approximation, the amplification rate increases with the rotation frequency and tends to infinity at the dynamo threshold. We used this fact to determine the dynamo threshold from the best fit of the magnetic field and the coil voltage. In this way, we found a critical rotation frequency $\Omega_c \approx 7 \pm 0.2\,\mathrm{Hz}$, which is somewhat larger than the actual saturation frequency observed in the third run. This is consistent with the numerical results which showed that the transient effects result in the best-fit value being somewhat higher than the actual dynamo threshold. On the other hand, this experimental result is somewhat lower than the theoretical prediction $\Omega_c \approx 8.2\,\mathrm{Hz}$ corresponding to the minimal critical magnetic Reynolds number $Rm \approx 35$ for a negligible contact resistance [17]. This difference is likely due to the very approximate nature of the current sheet model which was used to evaluate the dynamo threshold. In particular, due to the strongly uniform radial magnetic flux distribution (see Fig. 9), the total magnetic flux through the disc may be larger than theoretically predicted because the effective inner radius of the disc is smaller than that of the coil. The critical rotation rate can be reduced further by optimizing the inner and outer disc radii which were originally chosen to be the same as those of the coil.

Acknowledgements. We are grateful to Adrian Pérez, Carla Bello and and Manuel Valencia for the technical support.

Funding. This work was supported by the National Council of Science and Technology of Mexico (CONACYT) through grant CB-168850 and the National Polytechnic Institute (IPN) through grants SIP-20211736 and SIP-20220849.

References

1 Bullard E. 1955 The stability of a homopolar dynamo. *Proc. Camb. Phil. Soc.* **51**, 744–760.
2 Moffatt HK. 1978 *Magnetic field generation in electrically conducting fluids*. Cambridge monographs on mechanics and applied mathematics. Cambrige.
3 Beck R, Brandenburg A, Moss D, Shukurov A, Sokoloff D. 1996 Galactic magnetism: recent developments and perspectives. *Annu. Rev. Astron. Astrophys.* **34**, 155–206.
4 Gailitis A, Lielausis O, Platacis E, Dement'ev S, Cifersons A, Gerbeth G, Gundrum T, Stefani F, Christen M, Will G. 2001 Magnetic field saturation in the Riga dynamo experiment. *Phys. Rev. Lett.* **86**, 3024.

5 Stieglitz R, Müller U. 2001 Experimental demonstration of a homogeneous two-scale dynamo. *Phys. Fluids* **13**, 561–564.

6 Monchaux R, Berhanu M, Bourgoin M, Moulin M, Odier P, Pinton JF, Volk R, Fauve S, Mordant N, Pétrélis F, Chiffaudel A, Daviaud F, Dubrulle B, Gasquet C, Marié L, Ravelet F. 2007 Generation of a Magnetic Field by Dynamo Action in a Turbulent Flow of Liquid Sodium. *Phys. Rev. Lett.* **98**, 044502.

7 Stefani F, Gailitis A, Gerbeth G, Giesecke A, Gundrum T, Rüdiger G, Seilmayer M, Vogt T. 2019 The DRESDYN project: liquid metal experiments on dynamo action and magnetorotational instability. *Geophys. Astrophys. Fluid Dyn.* **113**, 51–70.

8 Rädler K, Rheinhardt M. 2002 Can a disc dynamo work in the laboratory?. *Magnetohydrodynamics* **38**, 211–217.

9 Dormy E, Soward AM. 2007 *Mathematical aspects of natural dynamos*. CRC.

10 Lorrain P, Lorrain F, Houle S. 2006 *Magneto-fluid dynamics: fundamentals and case studies of natural phenomena*. Springer.

11 Inall E, Hughes J. 1968 Homopolar Generator as the Energy Store for a Large Laser. *Nature* **220**, 1121–1121.

12 Maribo D, Sondergaard N. 1987 Further studies of a low-melting point alloy used in a liquid metal current collector. *IEEE Trans. Components, Hybrids Manuf. Technol.* **10**, 452–455.

13 Maribo D, Gavrilash M, Reilly PJ, Lynch WA, Sondergaard NA. 2010 Comparison of Several Liquid Metal Sliding Electric Contacts. In *56th IEEE Holm Conf. on Electrical Contacts* pp. 1–7.

14 Herzenberg A. 1958 Geomagnetic dynamos. *Phil. Trans. R. Soc. Lond. A* **250**, 543–583.

15 Lowes F, Wilkinson I. 1963 Geomagnetic dynamo: a laboratory model. *Nature* **198**, 1158–1160.

16 Lowes F, Wilkinson I. 1968 Geomagnetic dynamo: an improved laboratory model. *Nature* **219**, 717–718.

17 Priede J, Avalos-Zúñiga R. 2013 Feasible homopolar dynamo with sliding liquid-metal contacts. *Phys. Lett. A* **377**, 2093–2096.

18 Plunian F, Alboussière T. 2020 Axisymmetric dynamo action is possible with anisotropic conductivity. *Phys. Rev. Res.* **2**, 013321.

19 Alboussière T, Plunian F, Moulin M. 2022 Fury: an experimental dynamo with anisotropic electrical conductivity. *arXiv preprint arXiv:2206.00063*.

20 Avalos-Zúñiga R, Priede J, Bello-Morales C. 2017 A homopolar disc dynamo experiment with liquid metal contacts. *Magnetohydrodynamics* **53**, 341–348.

21 Moffatt HK. 1979 A self-consistent treatment of simple dynamo systems. *Geophys. Astrophys. Fluid Dyn.* **14**, 147–166.

22 Hughes A, Drury B. 2019 *Electric motors and drives: fundamentals, types and applications*. Newnes 5th edition.